Research in Astronomy and Astrophysics, 25:105005 (8pp), 2025 October
https://doi.org/10.1088/1674-4527/adf603
CSTR: 32081.14.RAA.adf603
© 2025. National Astronomical Observatories, CAS and IOP Publishing Ltd. All rights, including for text and data mining, AI training, and similar technologies, are reserved. Printed in China.

Relationship between the Detection Rates of Mg II Absorption Lines and [O III] Emission Line Asymmetries

Xing-Long Peng, Wei-Rong Huang, Zhi-Fu Chen, Zhe-Geng Chen, and Zhi-Wen Wang
School of Physics and Electronic Information, Guangxi Minzu University, Nanning 530006, China; w.r.huang@gxmzu.edu.cn
Received 2025 February 28; revised 2025 July 15; accepted 2025 July 23; published 2025 August 26

Abstract

This study investigates the relationship between the detection rates of Mg II absorption lines and the asymmetries of [O III] emission lines. We first select 21,364 quasars from the Sloan Digital Sky Survey DR12Q exhibiting prominent [O III] emission lines, of which 351 quasars have Category 1 Mg II absorption lines ($4365 \leqslant v_{\rm r} \leqslant 10{,}000\,{\rm km\,s^{-1}}$) and 518 quasars have Category 2 Mg II absorption lines ($610 \leqslant v_{\rm r} \leqslant 4365\,{\rm km\,s^{-1}}$). Subsequently, we quantify the asymmetries of [O III] emission lines using the velocity offset δv, and find that the detection rates of Category 1 Mg II absorption lines (predominantly intervening absorbers) show no correlation with the blueshifted asymmetries of [O III] emission lines, whereas the detection rates of Category 2 Mg II absorption lines (primarily outflow and intervening absorbers) increase with rising δv. Finally, we discuss the results from two perspectives: quasar evolutionary stages and acceleration mechanisms driven by radiation pressure.

Key words: ISM: jets and outflows – (ISM:) evolution – galaxies: active

1. Introduction

The accretion of supermassive black holes in active galactic nuclei (AGNs) releases vast amounts of energy in the form of radiation, winds, and jets. These energetic outputs interact with the surrounding interstellar medium (ISM), leading to the heating or ejection of gas. Such AGN feedback has the potential to alter star formation activity and gas dynamics within galaxies, impede gas accretion onto central black holes, and consequently regulate the evolutionary of galaxies (e.g., Heckman & Kauffmann 2006; Fabian 2012; Heckman & Best 2014, and therein). Previous studies have reported that AGNs can exert both negative feedback (e.g., Herrera-Camus et al. 2020; Fluetsch et al. 2021; Chen et al. 2022; Garofalo et al. 2023) and positive feedback (e.g., Carniani et al. 2016; Zhang 2021; Bessiere & Ramos Almeida 2022) on their host galaxies. However, an ongoing debate persists regarding whether AGN feedback predominantly acts as a positive or negative influence on star formation activity and galactic environments.

The narrow-line region (NLR) of AGNs, approximately situated between 0.1 and several kpc from the central black hole, plays a crucial role in the study of AGN feedback (e.g., Osterbrock & Ferland 2006; Heckman & Best 2014; Zheng 2020). This region typically exhibits narrow and intense emission lines in the optical spectrum (e.g., [O III]). If there is no additional influence, the movement of gas clouds within NLRs is virial, governed by the gravitational forces of the host galaxy, resulting in symmetric narrow emission line (NEL) profiles. This symmetrical profile is often referred to as the core component of the NEL. AGN feedback may disrupt the virial motion of the gas clouds within NLRs, leading to a blueshifted component overlain on the core component (e.g., Wang et al. 2016; Zhang 2021). Consequently, the NEL possibly exhibits an asymmetrical profile at the blue wing when the gas accelerates into an outflow and is illuminated by AGN. If the magnitude and intensity of the outflow are substantial, it may exert a feedback effect on the NLRs. Thus, the blueshifted component of NELs is often employed as a proxy to characterize the properties of AGN outflows (e.g., Zamanov et al. 2002; Holt et al. 2008; Peng et al. 2014; DiPompeo et al. 2018), where the outflows are the bridge of AGN feedback.

In the spectra of quasars, absorption features physically associated with quasar systems are referred to as associated absorption lines (AALs; e.g., Bahcall & Salpeter 1966; Shklovsky 1967; Weymann et al. 1981). These AALs typically have redshifts close to that of the quasar system. They may originate from outflows or winds driven by the central regions of quasars (intrinsic absorption lines) (e.g., Murray et al. 1995; Hamann et al. 1997; Ganguly et al. 2007; Laha et al. 2021), or they may arise from the host galaxy and its surrounding environment (environment absorption lines) (e.g., Crenshaw et al. 2003; Chen et al. 2018a; He et al. 2024). In contrast to AALs, intervening absorption lines usually originate from gas clouds that are located far from the quasar system and have no direct physical connection to it (e.g., York et al. 2006). The redshift of these absorbing clouds is significantly lower than that of the quasar system. The properties of AALs are linked to the gas distribution, density, ionization, dynamics, and evolutionary stage of the quasar host. Consequently, AALs serve as a valuable tool for probing the intrinsic properties of quasars (e.g., Hamann & Ferland 1999; Wise et al. 2004;

Vanden Berk et al. 2008; Tumlinson et al. 2017; Chen et al. 2020, 2022, 2023).

Both blueshifted [O III] emission lines and AALs can be used to trace outflows. The blueshifted [O III] emission lines primarily trace ionized gas in the NLR affected by AGN radiation and outflows, providing evidence of kinematic disturbances within the NLR (Komossa et al. 2008; Harrison et al. 2014; Xu & Wang 2022). AALs originating from outflows directly probe the gas ejected from the central regions of quasars, revealing the overall physical state and evolutionary characteristics of the quasar system (Hamann et al. 2012; Chen et al. 2022; Peng et al. 2024). The blueshifted [O III] emission lines and AALs offer complementary perspectives for a comprehensive understanding of AGN feedback mechanisms.

Utilizing the quasar spectra from the Twelfth Data Release (DR12Q; Pâris et al. 2017) of the Sloan Digital Sky Survey (SDSS; York et al. 2000), Chen et al. (2018b) systematically search for Mg II $\lambda\lambda$2796,2803 narrow absorption lines in the spectral regions surrounding Mg II λ2798 emission lines, which yields a sample of 17,316 Mg II absorption lines with relative velocity[1] $\upsilon_{\rm r} < 10{,}000\,{\rm km\,s^{-1}}$. This large sample of Mg II absorption lines offers a unique opportunity to investigate the feedback effect of quasars on their host galaxies. In this paper, we utilize the quasar spectra from the SDSS DR12Q and the Mg II absorption lines cataloged by Chen et al. (2018b) to explore the relationship between the detection rate of Mg II absorption lines and the asymmetry of the [O III] emission line. In this paper, we adopt the ΛCDM cosmology with $\Omega_m = 0.3$, $\Omega_\Lambda = 0.7$, and $H_0 = 70\,{\rm km\,s^{-1}\,Mpc^{-1}}$.

2. Quasar Sample and Spectral Analysis

2.1. Quasar Sample

The SDSS (York et al. 2000) is a comprehensive multi-band imaging and spectroscopic survey conducted using a 2.5 m optical telescope at the Apache Point Observatory. This telescope is equipped with the SDSS/BOSS spectrometer and is capable of simultaneously acquiring spectra of multiple targets through fiber optic technology (Gunn et al. 2006; Abazajian et al. 2009; Ahn et al. 2012). The SDSS spectrometer covers a wavelength range of 3800–9200 Å, while the BOSS spectrometer extends this range to 3600—10400 Å, with both spectrometers achieving a spectral resolution of $R \sim 2000$.

Chen et al. (2018b) systematically searched for Mg II $\lambda\lambda$2796,2803 narrow absorption lines in the quasar spectra from the SDSS DR12Q. Consequently, our sample is restricted to the quasars included in the SDSS DR12Q. To ensure that the [O III] λ5007 emission lines are covered by the SDSS spectra, we impose the following criteria: for quasars obtained during the SDSS-I/II stages, we require that $3800/2600 \leqslant (1 + z_{\rm em}) \leqslant 9200/5100$; for quasars acquired during the SDSS-III stage, the criterion is $3600/2600 \leqslant (1 + z_{\rm em}) \leqslant 10{,}400/5100$, where $z_{\rm em}$ is the "best redshift" taken from Lyke et al. (2020). To further ensure data quality, we select quasar spectra with a median signal-to-noise ratio (SNR) greater than 5. We also require that the quasar spectra cover the range from the Mg II emission line to its blue wing at $\upsilon_{\rm r} = 10{,}000\,{\rm km\,s^{-1}}$. Based on these criteria, our final sample comprises 21,364 quasars from the SDSS DR12Q. We proceed to measure the [O III] emission lines for these quasars in the subsequent section.

2.2. Spectral Analysis

The spectral fitting processes and methodologies employed in our analysis are consistent with those utilized by Shen et al. (2011) and Chen et al. (2018c, 2019). In the first step, the quasar spectra are corrected for Galactic extinction using reddening measurements from Schlafly & Finkbeiner (2011) and the Milky Way extinction curve developed by Cardelli et al. (1989). The spectra are then shifted to the quasar's rest frame using the best redshifts provided by Lyke et al. (2020). We aim to the parameters of the [O III] $\lambda\lambda$4959,5007 emission lines. Therefore, in the second step, we fit a local power-law continuum ($f_\lambda = A\lambda^a$) in conjunction with an iron template (Vestergaard & Wilkes 2001; Vestergaard & Peterson 2006) over the spectral data within the wavelength windows [4400, 4800] Å and [5100, 5550] Å. Figure 1 illustrates the fitting of the power-law continuum and iron emissions. In the third step, we subtract the fitted power-law continuum and iron emissions from the quasar spectra (as depicted by the green lines in the top panels of Figure 1) and employ multiple Gaussian functions to model the [O III] $\lambda\lambda$4959,5007 and Hβ emission lines using the spectral data within [4700, 5100] Å. The fitting processes of emission lines are detailed as follows:

1. The [O III] $\lambda\lambda$4959,5007 emission lines are modeled using two pairs of Gaussian functions; one pair, with FWHM $\leqslant 1200\,{\rm km\ s^{-1}}$, represents the core components, while the other pair, with FWHM $\leqslant 2500\,{\rm km\,s^{-1}}$, accounts for the blueshifted component (e.g., Peng et al. 2014; Chen et al. 2018c). Each [O III] doublet is constrained by a flux ratio of $F(5007)/F(4959) = 3{:}1$.
2. We utilize four Gaussian functions to represent the Hβ emissions, where three functions with FWHM $\geqslant 1200\ {\rm km\,s^{-1}}$ model the broad components, and one function with FWHM $< 1200\,{\rm km\,s^{-1}}$ accounts for the narrow component.
3. The velocity offset and line width are constrained to be identical for the narrow component of Hβ and the core component of [O III]. Moreover, the velocity offset and line width for the blueshifted components of the [O III] $\lambda\lambda$4959,5007 doublet are also set to be the same.

[1] Relative velocity $\upsilon_r = \frac{(1+z_{\rm em})^2 - (1+z_{\rm abs})^2}{(1+z_{\rm em})^2 + (1+z_{\rm abs})^2} \times c$, where c is the speed of light.

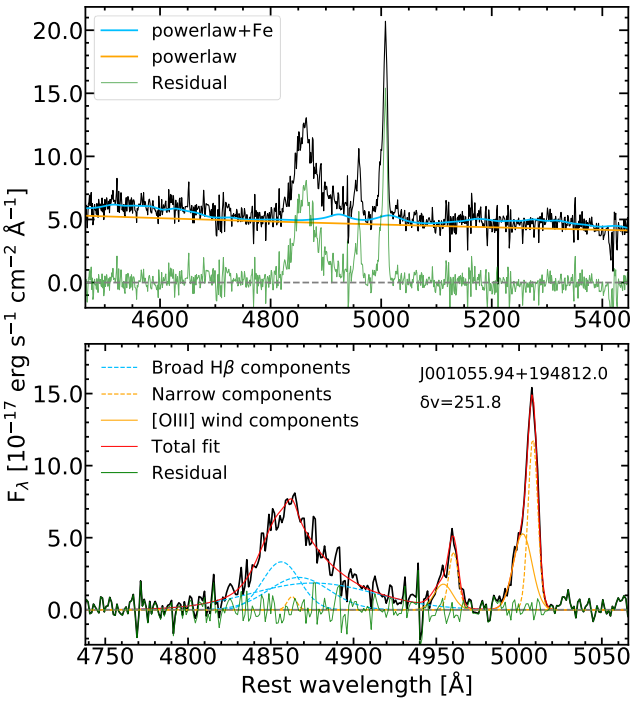


Figure 1. The quasar spectrum of SDSS J001055.94 +194812.0. Upper panel: the orange solid line represents the fitted power-law continuum, while the blue solid line represents the combined fit of the power-law plus iron template. The green solid line depicts the spectrum after subtracting the combined fit of the power-law and iron template. Lower panel: the blue dashed line illustrates the broad component of Hβ, the orange dashed line represents the narrow Hβ and core [O III] components, and the orange solid line indicates the blueshifted component of [O III]. The red solid line shows the sum of all Gaussian function fits. The green solid line illustrates the residual spectrum, which is obtained by subtracting the red solid line from the original spectrum.

The spectra fits are visually inspected one by one. Figure 1 provides an example of the fitted [O III] and Hβ emission lines as well. We exclude quasars with $f_{[\mathrm{O\ III}]\lambda5007} < 5\sigma_f$, where $f_{[\mathrm{O\ III}]\lambda5007}$ denotes the integral flux of the [O III] λ5007 emission line, encompassing both the core and blueshifted components, and σ_f represents the corresponding uncertainty. Additionally, we discard poorly fitted [O III] emission lines by visual inspection, due to subpar spectral data quality. Ultimately, we compile a sample of 21,364 quasars displaying obvious [O III] emission lines, the redshifts of which are presented in Figure 2.

Among the 21,364 quasars exhibiting notable [O III] emission lines, we find 869 quasars with obvious Mg II absorption lines within the range of $610 \leqslant \upsilon_r \leqslant 10{,}000\ \mathrm{km\ s^{-1}}$, which have been confirmed through visual inspection. The redshifts of these Mg II absorption lines are also displayed in Figure 2.

Using the measurements of the broad Hβ emission lines, we compute the virialized mass of the black hole (M_{BH}) using the following equation:

$$\log\left(\frac{M_{\mathrm{BH}}}{M_\odot}\right) = a + b\log\left(\frac{\lambda L_\lambda}{10^{44}\ \mathrm{erg\ s^{-1}}}\right) + 2\log\left(\frac{\mathrm{FWHM}}{\mathrm{km\ s^{-1}}}\right), \quad (1)$$

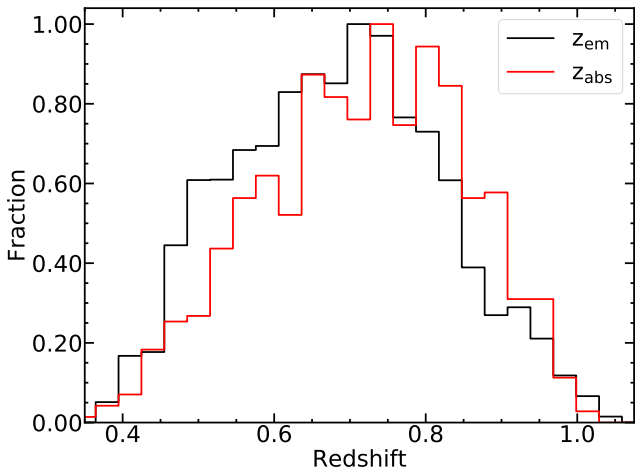


Figure 2. The distribution of redshifts. The black line denotes the redshifts of quasars, while the red line represents the redshifts of detected Mg II absorption lines.

where λL_λ represents the continuum luminosity at 5100 Å and FWHM is the full width at half maximum of broad Hβ emission line profile (fitted with three Gaussian components, each requiring a FWHM $\geqslant 1200\ \mathrm{km\ s^{-1}}$). The calibration coefficients a and b are set to (6.96, 0.50), as taken from Chen et al. (2018c). The Eddington ratio can be derived from the equation $\lambda_{\mathrm{Edd}} = L_{\mathrm{bol}}/L_{\mathrm{Edd}}$, where $L_{\mathrm{bol}} = 9.26\,L_{5100}$ and $L_{\mathrm{Edd}} = 1.26 \times 10^{38}(M_{\mathrm{BH}}/M_\odot)\ \mathrm{erg\ s^{-1}}$.

2.3. Parameterization of the [O III] Emission Line Asymmetry

Using the method adopted by Wang et al. (2016), we quantify the asymmetry of the [O III] emission line with the velocity offset δv. The δv is calculated as follows:

$$\delta v = -\frac{\sum_1^n a_k(\upsilon_k - \upsilon_p)}{\sum_1^n a_k}, \quad (2)$$

where, for the fitting of the [O III] λ5007 emission line, υ_p is the velocity of the peak flux. The terms a_k and υ_k denote the fitting flux and velocity of the kth spectral data used to fit the [O III], respectively. n represents the number of fitting fluxes that describe the [O III] emission line and have a strength greater than zero. According to Equation (2), positive and negative values of δv signify blueshifted and redshifted asymmetries, respectively. A larger value of δv indicates a more pronounced blue asymmetrical profile. The resulting values of δv are illustrated in Figure 3.

2.4. Mg II Absorption Lines at Different Relative Velocities

Chen et al. (2018b) employed three Gaussian profiles with peak velocities and standard deviations (v_0, σ) of (−1000, 1799), (0, 305) and (1023, 1671) $\mathrm{km\ s^{-1}}$, to characterize the

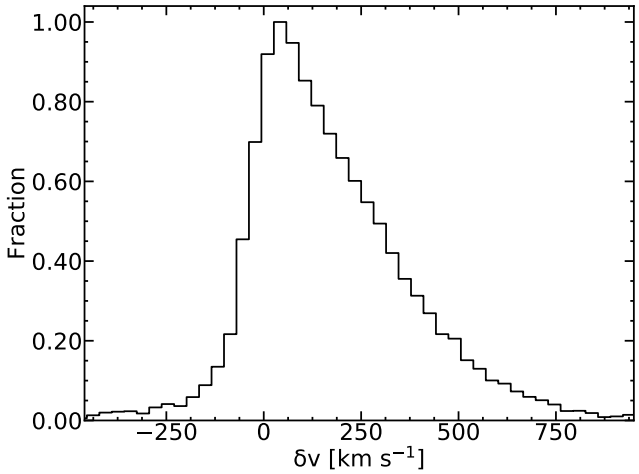


Figure 3. The δv distribution for 21,364 quasars within our sample.

relative velocity (υ_r) distributions of inflow, environment, and outflow Mg II absorbers, respectively (see their Figure 3). Additionally, they modeled the intervening absorbers using a constant function ($y = C$) across the range $\upsilon_r \geqslant 0$, where C is fixed to the average absorber count at $\upsilon_r > 6000\,\mathrm{km\,s^{-1}}$. In this study, we divide the Mg II absorption lines into two categories based on υ_r ranges:

1. Category 1 ($4365 \leqslant \upsilon_r \leqslant 10{,}000\,\mathrm{km\,s^{-1}}$): Mg II absorption lines with υ_r exceeding $4365\,\mathrm{km\,s^{-1}}$(the outflow absorber's peak υ_r plus 2σ) are designated as Category 1. The fractional contributions of inflow, environment, outflow, and intervening absorbers are quantified as 0.03%, $<10^{-6}$%, 1.97%, 98%, respectively, indicating that this category is dominated by intervening absorbers.
2. Category 2 ($610 \leqslant \upsilon_r < 4365\,\mathrm{km\,s^{-1}}$): The υ_r boundaries are defined using 2σ limits, with the left boundary ($610\,\mathrm{km\,s^{-1}}$) set at the environment absorber's peak υ_r plus 2σ ($0 + 2 \times 305\,\mathrm{km\,s^{-1}}$), and the right boundary ($4365\,\mathrm{km\,s^{-1}}$) at the outflow absorber's peak υ_r plus 2σ ($1023 + 2 \times 1671\,\mathrm{km\,s^{-1}}$). The fractional contributions are 3.3%, 1.2%, 44.8%, and 50.7% for inflow, environment, outflow, and intervening absorbers, respectively, indicating this category is dominated by outflow and intervening absorbers (combined 95.5%).

Among the 21,364 quasars, 351 exhibit Mg II absorption lines of Category 1, while 518 display Mg II absorption lines of Category 2. Figure 4 shows the examples of Mg II absorption lines from Category 1 and Category 2.

3. Results

We first sort the sample (21,364 quasars) in ascending order of δv, then partition the sorted sample into consecutive bins, each containing 800 quasars (see Table A1 for details). The

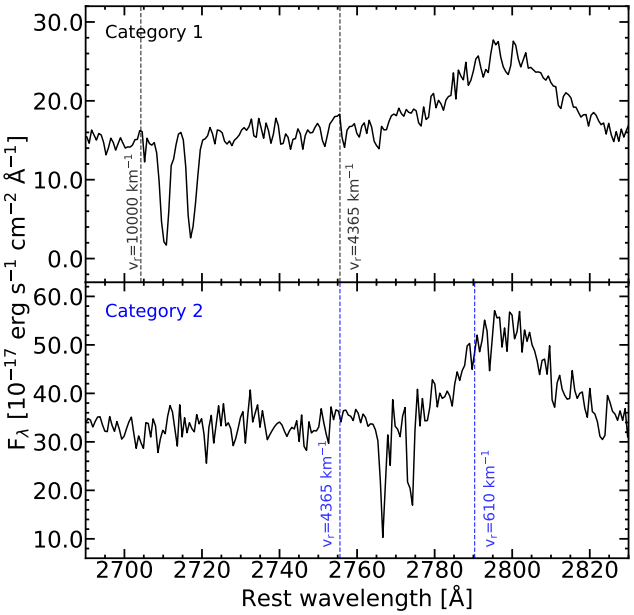


Figure 4. Examples of Mg II absorption lines from Category 1 (top, spec-5361-55973-0234) and Category 2 (bottom, spec-1975-53734-0311).

detection rate f_c of Mg II absorption lines is calculated for each bin:

$$f_c = \frac{N_{abs}}{N_{QSO}} = \frac{\sum_{i=1}^{N} X(i)}{N}, \quad (3)$$

where N_{abs} is the number of quasars associated with Mg II absorbers, N_{QSO} is the number of quasars. $X = 0$ or 1 indicates the absence or presence of Mg II absorption lines in the ith quasar spectrum, respectively. N represents the number of spectra in each bin of quasars, and the uncertainty of detection rate (σ_{fc}) is estimated using binomial statistics.

The f_c of Mg II absorption lines from different categories as a function of δv is presented in Figure 5. For Category 1, the f_c remains constant with varying δv. For Category 2, the f_c shows a gradual increase with increasing δv. Within $\delta v = 200$–$600\,\mathrm{km\ s^{-1}}$, the linear fit yields a correlation coefficient $r = 0.996$ ($p < 10^{-3}$) with the relation $y = (8.6 \pm 0.5) \times 10^{-5}x + (0.003 \pm 0.002)$ (blue line in Figure 5). Since Category 1 contains 98% intervening absorbers, the flat trend primarily reflects the behavior of intervening absorbers. Category 2 consists mainly of intervening and outflow absorbers. As the Mg II detection rate of the intervening absorbers shows no variation with δv, the increasing trend of Mg II detection rate with blueshifted asymmetry in Category 2 is predominantly driven by the outflow absorbers.

A larger δv might lead to a higher SNR, which can increase the f_c of absorption lines. To quantify the contribution of SNR, we calculate the median SNR of spectrum (SNR_m) within the υ_r range of Category 2 for each δv bin (see Figure 6). Within $\delta v = 200$–$600\ \mathrm{km\ s^{-1}}$, the SNR_m of Category 2 exhibits an

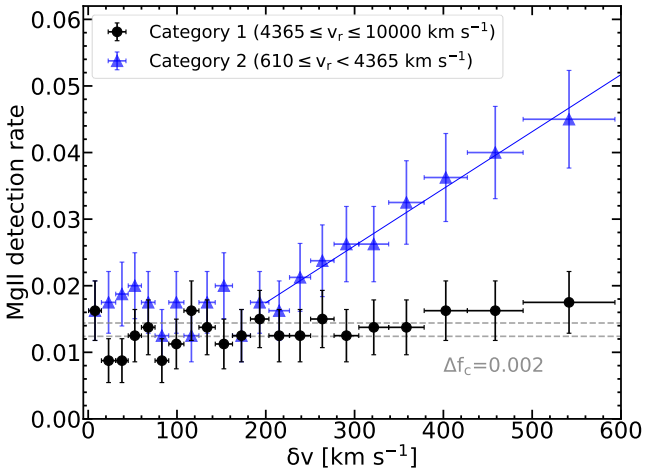


Figure 5. The detection rates (f_c) of Mg II absorption lines as a function of δv. Each point represents a bin containing 800 quasars. The region between the two dashed lines represents a reference value of $\Delta f_c = 0.002$. The blue line shows the linear fit: $y = (8.6 \pm 0.5) \times 10^{-5}x + (0.003 \pm 0.002)$.

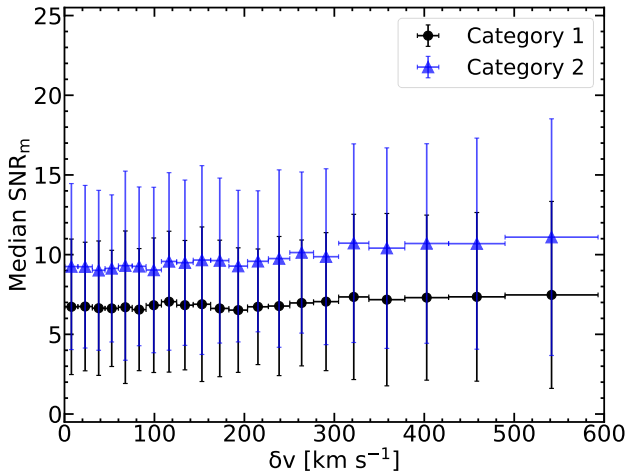


Figure 6. The median $\mathrm{SNR_m}$ in different δv bins. The error bars represent the standard deviation of each bin.

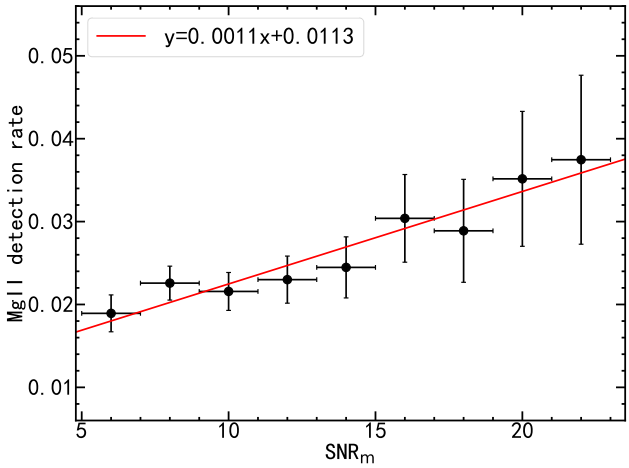


Figure 7. The relationship between the f_c of Category 2 and $\mathrm{SNR_m}$ within $610 \leqslant v_r \leqslant 4365$ km s^{-1}. The error bars represent the standard error of each bin.

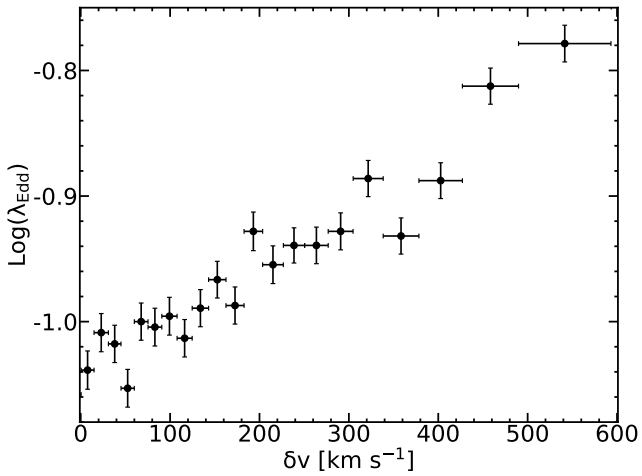


Figure 8. The relationship between the λ_{Edd} and δv. The error bars represent the standard error of each bin.

increase of ∼1.5 (from 9.581 to 11.10). Furthermore, we use Category 2 to determine the relationship between SNR and f_c and yield a relation $y = 0.0011x$–0.0113 (Figure 7), indicating that a change in $\mathrm{SNR_m}$ of 1.5 for Category 2 could result in $\Delta f_c \approx 0.002$. In Figure 5, the corresponding Δf_c for Category 2 is actually ∼0.029 (=0.045–0.016). Thus, the trend of Category 2 presented in Figure 5 is not likely caused by the difference in SNR.

4. Discussions

Previous studies have found a strong correlation between the asymmetry of the [O III] profile and λ_{Edd} (e.g., Christopoulou et al. 1997; Bian et al. 2005; Boroson 2005; Wang et al. 2011, 2018; Zhang et al. 2011; Wang & Xu 2015; Rakshit & Woo 2018; Jin et al. 2023). In addition, the Eddington ratio is likely related to the evolutionary stage of AGNs, as they tend to exhibit higher λ_{Edd} during the early phases of their evolution (e.g., Grupe 2004; Hopkins & Hernquist 2009; Wu 2009; Cao 2010). In Figure 8 we also show the asymmetry of the [O III] profiles is moderately correlated with the λ_{Edd}. λ_{Edd} rises with a growth in δv, which is consistent with previous works.

If AGNs exhibit a higher λ_{Edd} during the early phases of their evolution, AGNs with larger values of δv tend to be in the earlier evolutionary stage. Therefore, Figure 5 may indicate that the Mg II absorbers from different categories likely exhibit distinct evolutionary behaviors. For Category 1, the f_c remains constant with varying δv. This phenomenon is natural since the intervening absorption line systems are located far beyond the quasar systems and are unaffected by changes in the intrinsic

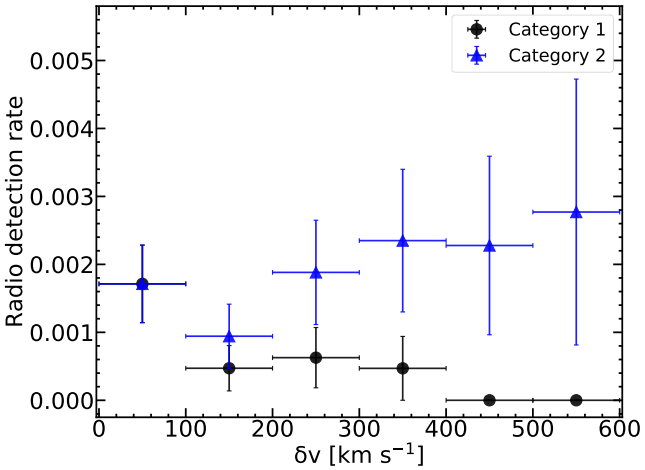


Figure 9. The radio detection rate of quasars in different δv bins. The error bars represent the standard error of each bin. Note: the radio detection rates of the two rightmost bins are zero, and there are no error bars.

properties of the quasars. For Category 2, the f_c shows a gradual decrease with decreasing δv. In the early stages of evolution, it is believed that quasars have enough gas interacting with the jets/winds. The jets/winds can potentially push the surrounding gas to high outflow speeds, leading to a higher percentage of quasars showing outflow absorption lines (see the right side of Figure 5). However, as the jets/winds develop, they progressively clear the surrounding gas, resulting in insufficient gas to interact with them (e.g., Mukherjee et al. 2016, 2018; Meenakshi et al. 2022). Consequently, in the later stages of evolution, a smaller percentage of quasars show detectable outflow absorption lines (see the left side of Figure 5).

If the Mg II absorbing outflows originate from interactions between jets or stellar winds and the ambient medium, one would expect high-velocity outflows to be accompanied by enhanced radio emission. To test this hypothesis, we examine the correlation between the radio detection rate and the [O III] δv (Figure 9) by cross-matching Category 1 and Category 2 with the radio catalog[2] from Very Large Array Sky Survey (VLASS; Lacy et al. 2020) using a 5″ search radius, yielding 32 and 50 radio-detected quasars, respectively. For Category 2, the radio detection rate increases with [O III] δv, with a correlation coefficient of $r \approx 0.89$ ($p \approx 0.02$) for $\delta v = 0$–$600\,\mathrm{km\,s^{-1}}$, supporting the scenario in which jet/wind-ISM interactions generate radio emission (e.g., Christopoulou et al. 1997; Bessiere et al. 2024; Liao et al. 2024). By contrast, for Category 1 (dominated by intervening absorbers), an elevated radio detection rate only exhibits in the range $\delta v = 0$–$100\,\mathrm{km\,s^{-1}}$ bin, which is likely a statistical fluctuation owing to the small sample size. Over $\delta v = 100$–$600\,\mathrm{km\,s^{-1}}$, the radio detection rate remains essentially flat, as expected if the intervening absorbers are not correlated to δv.

However, although a positive correlation exists between the λ_{Edd} and the δv of [O III] emission lines, it is not appropriate to directly use the δv as a proxy for the quasar's age. This is primarily due to the limited dynamic range in the λ_{Edd}. In the following paragraph, we discuss it from the perspective of radiation pressure-driven outflows (e.g., Proga et al. 2000; Proga & Kallman 2004). For Category 1, the detection rates of Mg II absorption lines remain invariant with respect to the blueshifted asymmetries (δv) of the [O III] emission lines. This is attributed to the very small influence of central radiation pressure, as the intervening absorption lines are spatially distant from the central engine. In contrast, for Category 2, a significant positive correlation emerges between the f_c of Mg II absorption lines and the δv of [O III] emission lines (Figure 5). As previously discussed, this trend is primarily driven by the outflow Mg II absorbers. Simultaneously, the δv of [O III] exhibits a significant correlation with the λ_{Edd} (correlation coefficient $r = 0.948$, $p = 7 \times 10^{-11}$; Figure 8). Based on these correlations, we propose that for Category 2, the rising trend of f_c with increasing δv may be closely linked to the outflow acceleration mechanism driven by radiation pressure. Typically, the blueshift of [O III] line is used as a tracer of NLR outflows (e.g., Zamanov et al. 2002; Peng et al. 2014; Schmidt et al. 2018). Here, the positive correlation between δv and the λ_{Edd} aligns with predictions of outflow acceleration powered by radiation pressure (e.g., Mas-Ribas 2019; He et al. 2022). In general, a higher λ_{Edd} implies stronger radiation pressure from the accretion disk. As the λ_{Edd} increases, enhanced radiation pressure can drive and accelerate the disk wind (e.g., Elvis 2000; Chen et al. 2024; Vivek & Wylezalek 2025), thereby amplifying dynamical disturbances of the gas from the BLR out to NLR scales, manifested as an increase in [O III] δv.

According to Xu et al. (2020), the [O III] emission line and broad-absorption-line outflows may represent different manifestations of the same wind. Building on this concept, we extend this interpretation to narrow Mg II absorption systems. If [O III] emitting gas and Mg II absorbers originate from the same wind, both would be subject to radiation-pressure-driven acceleration. Moreover, the increase in the f_c of the outflow Mg II absorption lines may reflect the spatial extension of the outflow during acceleration (He et al. 2022). When the Mg II outflow occupies larger regions, the probability that the line of sight intersects the absorbing gas increases. However, f_c remains constant for $\delta v = 0$–$200\,\mathrm{km\,s^{-1}}$, possibly due to the low velocity gas being gravitationally bound and unable to escape the central potential.

5. Summary

This study examines the relationship between the detection rates of Mg II absorption lines (f_c) and the asymmetries of [O III] emission lines (δv) in 21,364 quasars selected from

[2] Data from CIRADA_VLASS1QLv3.1_table1_components.csv, available at https://cirada.ca/catalogs.

SDSS. By categorizing Mg II absorption lines based on relative velocities (υ_r), we discover that Category 1 absorption lines ($4365 \leqslant \upsilon_r \leqslant 10{,}000\ \mathrm{km\ s^{-1}}$, predominantly intervening absorbers) show no correlation with [O III] δv, while Category 2 absorption lines ($610 \leqslant \upsilon_r \leqslant 4365\ \mathrm{km\ s^{-1}}$, primarily outflow and intervening absorbers) exhibit increased f_c with rising δv. From an evolutionary perspective, AGNs in early stages display higher Eddington ratios (λ_{Edd}) and δv, with abundant gas-jet/wind interactions, while later stages show reduced outflow Mg II absorbers as surrounding gas is cleared. The significant positive correlation between radio detection rate and δv for Category 2 absorbers further supports the scenario in which jet/wind-ISM interactions generate radio emission. From the perspective of radiation pressure-driven outflow acceleration, [O III] emission lines and Mg II absorption outflows may represent different manifestations of the same wind, with increased f_c reflecting spatial extension during acceleration.

Acknowledgments

We deeply thank the anonymous referee for their helpful and careful comments. This work is supported by the Scientific Research Project of Guangxi Minzu University (2023KJQD07), Guangxi Natural Science Foundation (2025GXNSFBA069287); the National Natural Science Foundation of China (12073007), the Guangxi Natural Science Foundation (2024GXNSFDA010069; 2019GXNSFFA245008), and the Scientific Research Project of Guangxi University for Nationalities (2018KJQD01). The data that support the findings of this study are available at https://github.com/dataHL/07025. We thank SDSS for the public data. Funding for SDSS-III has been provided by the Alfred P. Sloan Foundation, the Participating Institutions, the National Science Foundation, and the U.S. Department of Energy Office of Science. The SDSS-III website is http://www.sdss3.org/. SDSS-III is managed by the Astrophysical Research Consortium for the Participating Institutions of the SDSS-III Collaboration including the University of Arizona, the Brazilian Participation Group, Brookhaven National Laboratory, Carnegie Mellon University, University of Florida, the French Participation Group, the German Participation Group, Harvard University, the Instituto de Astrofisica de Canarias, the Michigan State/Notre Dame/JINA Participation Group, Johns Hopkins University, Lawrence Berkeley National Laboratory, Max Planck Institute for Astrophysics, Max Planck Institute for Extraterrestrial Physics, New Mexico State University, New York University, Ohio State University, Pennsylvania State University, University of Portsmouth, Princeton University, the Spanish Participation Group, University of Tokyo, University of Utah, Vanderbilt University, University of Virginia, University of Washington, and Yale University.

Appendix

We conduct tests by varying the υ_r range criteria for 'Category 2' in Figure 5 and find that the correlation between the Mg II detection rate and [O III] line asymmetry remains unchanged (see Figure A1). The data corresponding to Figures 5 and 6 are provided in Table A1.

Table A1
Data Corresponding to Figures 5 and 6

δv	f_c(Category 1)	f_c(Category 2)	$\mathrm{SNR_m}$(Category 1)	$\mathrm{SNR_m}$(Category 2)
[0.45, 14.9)	0.016 ± 0.0045	0.016 ± 0.0045	6.726	9.251
[14.9, 31.0)	0.009 ± 0.0033	0.018 ± 0.0046	6.744	9.242
[31.0, 45.1)	0.009 ± 0.0033	0.019 ± 0.0048	6.640	9.016
[45.1, 60.0)	0.013 ± 0.0039	0.020 ± 0.0049	6.626	9.135
[60.0, 75.3)	0.014 ± 0.0041	0.018 ± 0.0046	6.700	9.307
[75.3, 90.7)	0.009 ± 0.0033	0.013 ± 0.0039	6.551	9.266
[90.7, 107.8)	0.011 ± 0.0037	0.018 ± 0.0046	6.825	9.035
[107.8, 124.7)	0.016 ± 0.0045	0.013 ± 0.0039	7.049	9.573
[124.7, 143.1)	0.014 ± 0.0041	0.018 ± 0.0046	6.829	9.494
[143.1, 162.5)	0.011 ± 0.0037	0.020 ± 0.0049	6.888	9.660
[162.5, 182.8)	0.013 ± 0.0039	0.013 ± 0.0039	6.624	9.628
[182.8, 203.5)	0.015 ± 0.0043	0.018 ± 0.0046	6.520	9.280
[203.5, 226.7)	0.013 ± 0.0039	0.016 ± 0.0045	6.728	9.581
[226.7, 250.5)	0.013 ± 0.0039	0.021 ± 0.0051	6.774	9.753
[250.5, 276.9)	0.015 ± 0.0043	0.024 ± 0.0054	6.969	10.13
[276.9, 304.8)	0.013 ± 0.0039	0.026 ± 0.0057	7.051	9.870
[304.8, 338.4)	0.014 ± 0.0041	0.026 ± 0.0057	7.346	10.72
[338.4, 378.3)	0.014 ± 0.0041	0.033 ± 0.0063	7.174	10.41
[378.4, 427.0)	0.016 ± 0.0045	0.036 ± 0.0066	7.302	10.70
[427.0, 489.8)	0.016 ± 0.0045	0.040 ± 0.0069	7.351	10.69
[489.8, 593.4)	0.018 ± 0.0046	0.045 ± 0.0073	7.473	11.10

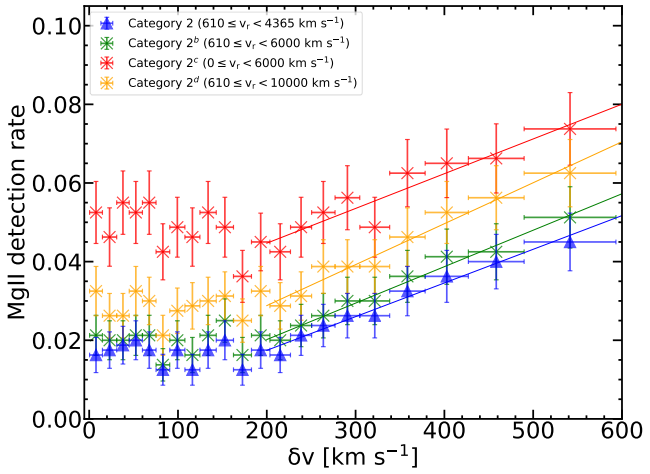


Figure A1. The detection rates (f_c) of Mg II absorption lines as a function of δv for Category 2. Within $\delta v = 200$–600 km s^{-1}, linear fits across different δv ranges yield strong correlations. For v_r = 610–6000 km s^{-1}, we obtain $r = 0.996$ ($p < 10^{-3}$) with $y = (9.3 \pm 0.5) \times 10^{-5}x + (0.002 \pm 0.002)$. Expanding to the range v_r = 0–6000 km s^{-1} gives $r = 0.929$ ($p < 10^{-3}$) and $y = (8.8 \pm 1.2) \times 10^{-5}x + (0.027 \pm 0.004)$, while extending to v_r = 610–10,000 km s^{-1} yields $r = 0.983$ ($p < 10^{-3}$) with $y = (10.4 \pm 0.7) \times 10^{-5}x + (0.008 \pm 0.003)$.

References

Abazajian, K. N., Adelman-McCarthy, J. K., Agüeros, M. A., et al. 2009, ApJS, 182, 543
Ahn, C. P., Alexandroff, R., Allende Prieto, C., et al. 2012, ApJS, 203, 21
Bahcall, J. N., & Salpeter, E. E. 1966, ApJ, 144, 847
Bessiere, P. S., & Ramos Almeida, C. 2022, MNRAS, 512, L54
Bessiere, P. S., Ramos Almeida, C., Holden, L. R., Tadhunter, C. N., & Canalizo, G. 2024, A&A, 689, A271
Bian, W., Yuan, Q., & Zhao, Y. 2005, MNRAS, 364, 187
Boroson, T. 2005, AJ, 130, 381
Cao, X. 2010, ApJ, 725, 388
Cardelli, J. A., Clayton, G. C., & Mathis, J. S. 1989, ApJ, 345, 245
Carniani, S., Marconi, A., Maiolino, R., et al. 2016, A&A, 591, A28
Chen, C., Hamann, F., Simon, L., & Barlow, T. 2018a, MNRAS, 481, 3865
Chen, Z.-F., Huang, W.-R., Pang, T.-T., et al. 2018b, ApJS, 235, 11
Chen, Z.-F., Pan, D.-S., Pang, T.-T., & Huang, Y. 2018c, ApJS, 234, 16
Chen, S., Laor, A., Behar, E., et al. 2024, ApJ, 975, 35
Chen, Z.-F., Qin, H.-C., Cai, J.-T., et al. 2023, ApJS, 265, 46
Chen, Z.-F., Qin, H.-C., Chen, Z.-G., et al. 2020, ApJ, 893, 25
Chen, Z.-F., Yi, S.-X., Pang, T.-T., et al. 2019, ApJS, 244, 36
Chen, Z., He, Z., Ho, L. C., et al. 2022, NatAs, 6, 339
Christopoulou, P. E., Holloway, A. J., Steffen, W., et al. 1997, MNRAS, 284, 385
Crenshaw, D. M., Kraemer, S. B., & Gabel, J. R. 2003, AJ, 126, 1690
DiPompeo, M. A., Hickox, R. C., Carroll, C. M., et al. 2018, ApJ, 856, 76
Elvis, M. 2000, ApJ, 545, 63
Fabian, A. C. 2012, ARA&A, 50, 455
Fluetsch, A., Maiolino, R., Carniani, S., et al. 2021, MNRAS, 505, 5753
Ganguly, R., Brotherton, M. S., Cales, S., et al. 2007, ApJ, 665, 990
Garofalo, D., Christian, D. J., Hames, C., et al. 2023, OJAp, 6, 27
Grupe, D. 2004, AJ, 127, 1799
Gunn, J. E., Siegmund, W. A., Mannery, E. J., et al. 2006, AJ, 131, 2332
Hamann, F., Barlow, T., Cohen, R. D., Junkkarinen, V., & Burbidge, E. M. 1997, in ASP Conf. Ser. 128, Mass Ejection from Active Galactic Nuclei, ed. N. Arav, I. Shlosman, & R. J. Weymann (San Francisco, CA: ASP), 19
Hamann, F., & Ferland, G. 1999, ARA&A, 37, 487
Hamann, F., Simon, L., Rodriguez Hidalgo, P., & Capellupo, D. 2012, in ASP Conf. Ser. 460, AGN Winds in Charleston, ed. G. Chartas, F. Hamann, & K. M. Leighly (San Francisco, CA: ASP), 47
Harrison, C. M., Alexander, D. M., Mullaney, J. R., & Swinbank, A. M. 2014, MNRAS, 441, 3306
He, Z., Chen, Z., Liu, G., et al. 2024, SCPMA, 67, 129512
He, Z., Liu, G., Wang, T., et al. 2022, SciA, 8, eabk3291
Heckman, T. M., & Best, P. N. 2014, ARA&A, 52, 589
Heckman, T. M., & Kauffmann, G. 2006, NewAR, 50, 677
Herrera-Camus, R., Janssen, A., Sturm, E., et al. 2020, A&A, 635, A47
Holt, J., Tadhunter, C. N., & Morganti, R. 2008, MNRAS, 387, 639
Hopkins, P. F., & Hernquist, L. 2009, ApJ, 698, 1550
Jin, S., Wang, J., Kong, M. Z., et al. 2023, ApJ, 950, 16
Komossa, S., Xu, D., Zhou, H., Storchi-Bergmann, T., & Binette, L. 2008, ApJ, 680, 926
Lacy, M., Baum, S. A., Chandler, C. J., et al. 2020, PASP, 132, 035001
Laha, S., Reynolds, C. S., Reeves, J., et al. 2021, NatAs, 5, 13
Liao, M., Wang, J., Ren, W., & Zhou, M. 2024, MNRAS, 528, 3696
Lyke, B. W., Higley, A. N., McLane, J. N., et al. 2020, ApJS, 250, 8
Mas-Ribas, L. 2019, ApJ, 885, 95
Meenakshi, M., Mukherjee, D., Wagner, A. Y., et al. 2022, MNRAS, 516, 766
Mukherjee, D., Bicknell, G. V., Sutherland, R., & Wagner, A. 2016, MNRAS, 461, 967
Mukherjee, D., Bicknell, G. V., Wagner, A. Y., Sutherland, R. S., & Silk, J. 2018, MNRAS, 479, 5544
Murray, N., Chiang, J., Grossman, S. A., & Voit, G. M. 1995, ApJ, 451, 498
Osterbrock, D. E., & Ferland, G. J. 2006, Astrophysics of Gaseous Nebulae and Active Galactic Nuclei (Sausalito, CA: Univ. Science Books)
Pâris, I., Petitjean, P., Ross, N. P., et al. 2017, A&A, 597, A79
Peng, X.-L., Chen, Z.-F., He, Z.-C., Pang, T.-T., & Wang, Z.-W. 2024, ApJ, 963, 3
Peng, Z.-X., Chen, Y.-M., Gu, Q.-S., & Zhang, K. 2014, RAA, 14, 913
Proga, D., & Kallman, T. R. 2004, ApJ, 616, 688
Proga, D., Stone, J. M., & Kallman, T. R. 2000, ApJ, 543, 686
Rakshit, S., & Woo, J.-H. 2018, ApJ, 865, 5
Schlafly, E. F., & Finkbeiner, D. P. 2011, ApJ, 737, 103
Schmidt, E. O., Oio, G. A., Ferreiro, D., Vega, L., & Weidmann, W. 2018, A&A, 615, A13
Shen, Y., Richards, G. T., Strauss, M. A., et al. 2011, ApJS, 194, 45
Shklovsky, J. 1967, ApJL, 150, L1
Tumlinson, J., Peeples, M. S., & Werk, J. K. 2017, ARA&A, 55, 389
Vanden Berk, D., Khare, P., York, D. G., et al. 2008, ApJ, 679, 239
Vestergaard, M., & Peterson, B. M. 2006, ApJ, 641, 689
Vestergaard, M., & Wilkes, B. J. 2001, ApJS, 134, 1
Vivek, M., & Wylezalek, D. 2025, A&A, 695, L22
Wang, J., Mao, Y. F., & Wei, J. Y. 2011, ApJ, 741, 50
Wang, J., & Xu, D. W. 2015, A&A, 573, A15
Wang, J., Xu, D. W., & Wei, J. Y. 2016, AJ, 151, 81
Wang, J., Xu, D. W., & Wei, J. Y. 2018, ApJ, 852, 26
Weymann, R. J., Carswell, R. F., & Smith, M. G. 1981, ARA&A, 19, 41
Wise, J. H., Eracleous, M., Charlton, J. C., & Ganguly, R. 2004, ApJ, 613, 129
Wu, Q. 2009, MNRAS, 398, 1905
Xu, X., & Wang, J. 2022, ApJ, 933, 110
Xu, X., Zakamska, N. L., Arav, N., Miller, T., & Benn, C. 2020, MNRAS, 495, 305
York, D. G., Adelman, J., Anderson, J. E., et al. 2000, AJ, 120, 1579
York, D. G., Khare, P., Vanden Berk, D., et al. 2006, MNRAS, 367, 945
Zamanov, R., Marziani, P., Sulentic, J. W., et al. 2002, ApJL, 576, L9
Zhang, K., Dong, X.-B., Wang, T.-G., & Gaskell, C. M. 2011, ApJ, 737, 71
Zhang, X.-G. 2021, MNRAS, 502, 2508
Zheng, W. 2020, ApJ, 892, 139